

# Aftershocks of the 2012 $M_w$ 7.6 Nicoya, Costa Rica, Earthquake and Mechanics of the Plate Interface

by Esteban J. Chaves,\* Laure Duboeuf, Susan Y. Schwartz, Thorne Lay, and Jonas Kintner

**Abstract** Subduction of the Cocos plate beneath the Nicoya Peninsula, Costa Rica, generates large underthrusting earthquakes with a recurrence interval of about 50 yrs. The most recent of these events occurred on 5 September 2012 ( $M_w$  7.6). A vigorous sequence of more than 6400 aftershocks was recorded by a local seismic network within the first four months after the mainshock. We determine locations and focal mechanisms for as many aftershocks as possible with  $M \geq 1.5$  occurring within the first nine days of the mainshock, all aftershocks with  $M \geq 3$  through the end of 2012, and all events with  $M \geq 4$  through the end of 2015. We determine faulting geometries using regional full waveform moment tensor (MT) inversion for the largest events ( $M \geq 4$ ) and  $P$ -wave first-motion polarities for smaller events, producing a mechanism catalog with 347 earthquakes. Sixty percent of these events are identified as underthrusting, and their locations are compared with spatial distributions of mainshock slip, afterslip, prior interplate seismicity, and slow-slip phenomena to better understand the mechanical behavior of the plate interface. Most of the aftershocks on the megathrust occur up-dip of the coseismic slip, where afterslip is large, and between coseismic slip and shallow slow-slip patches. The pattern of interplate seismicity during the interseismic period is similar to that for the aftershocks but does not extend to as great a depth. The coseismic slip extends even deeper than the interplate aftershocks, suggesting that the mainshock ruptured a strongly locked patch driving down-dip slip into the conditionally stable part of the deep plate interface that also hosts slow slip. About 80% of the aftershocks have one nodal plane oriented favorably to promote failure from static stress changes following the mainshock and early afterslip, whereas most others occur in regions of large afterslip.

*Electronic Supplement:* Tables of hypocenter location and focal mechanisms and selection criteria for underthrusting events and figures showing the Gutenberg–Richter distribution, regional moment tensor inversion, spatial distribution of earthquake activity, and temporal distribution of underthrusting events.

## Introduction

Aftershock studies of many large earthquakes indicate that most aftershocks occur outside of regions of large coseismic slip or at transitions from high to low slip (e.g., Hsu *et al.*, 2006; Asano *et al.*, 2011; Rietbrock *et al.*, 2012). Many studies tried to correlate aftershock occurrence with afterslip, with mixed results. However, few of these studies isolate the interplate aftershocks as needed to confidently evaluate the plate boundary behavior. For many recent megathrust events, detailed aftershock studies indicate that a significant fraction of the aftershocks occurred off the main

thrust interface (e.g., Ito *et al.*, 2004). Here we determine locations and focal mechanisms of aftershocks of the 5 September 2012  $M_w$  7.6 Nicoya Peninsula, Costa Rica, earthquake and isolate those that occur on the plate interface. We then compare their locations to the distributions of mainshock slip, afterslip, slow-slip events (SSEs), and interseismic interplate seismicity patterns to better understand the mechanical properties of the plate interface.

The 2012 earthquake ruptured a well-identified mature seismic gap that had previously ruptured in 1950. With the Nicoya Peninsula extending seaward, well out over the plate boundary, seismic and Global Positioning System (GPS) instrumentation was deployed in the gap several decades

\*Also at Observatorio Vulcanológico y Sismológico de Costa Rica (OVSI-CORI), Universidad Nacional, Apartado 1718-3000, Heredia 3000, Costa Rica.

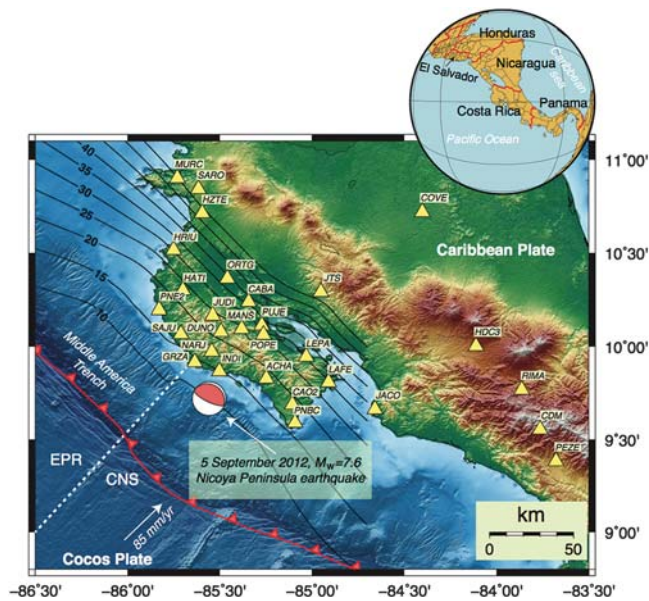


**Figure 1.** Map view showing the spatial distribution of the Nicoya Seismic Cycle Observatory and Volcanological and Seismological Observatory of Costa Rica (OVSICORI-UNA) seismic stations used in this study. Contour lines (DeShon *et al.*, 2006) indicate the depth to the top of the subducted slab. The dashed line represents the East Pacific Rise (EPR)–Cocos Nazca Spreading center (CNS) boundary (Barckhausen *et al.*, 2001). The epicentral location and focal mechanism of the 5 September 2012  $M_w$  7.6 Nicoya Peninsula earthquake are also indicated.

before the 2012 rupture. The late interseismic, coseismic, and postseismic phases of the earthquake cycle were thus all well recorded by local GPS and seismic networks. These data have been used to construct models of the interseismic strain accumulation on the plate interface (Feng *et al.*, 2012; Xue *et al.*, 2015; Kyriakopoulos and Newman, 2016), the distributions of coseismic slip (Yue *et al.*, 2013; Protti *et al.*, 2014; Liu *et al.*, 2015; Kyriakopoulos and Newman, 2016) and afterslip (Malservisi *et al.*, 2015), the timing and location of slow-slip and tremor events (Walter *et al.*, 2011; Dixon *et al.*, 2014), the foreshock behavior (Walter *et al.*, 2015), and interseismic seismicity patterns (Newman *et al.*, 2002; DeShon *et al.*, 2006; Hansen, 2006). Here, we generate a catalog of 347 focal mechanisms for well-located aftershocks and seek to better characterize the slip behavior of the plate interface in a region where past studies documented strong lateral variations in thermal structure, pore fluids, earthquake activity, and fault frictional behavior (Langseth and Silver, 1996; Audet and Schwartz, 2013). We also perform Coulomb stress-change calculations to compare all aftershock locations and mechanisms to static stress changes induced by the mainshock rupture.

### Tectonic Setting

Costa Rica is part of the Central America volcanic front, formed by subduction of the oceanic Cocos plate beneath the continental Caribbean plate along the Middle America trench

(MAT) at a rate of  $\sim 85\text{--}90$  mm/yr (DeMets *et al.*, 2010; Fig. 1). This rapid convergence rate generated magnitude 7+ earthquakes in 1853, 1900, 1950, and 2012 along the Nicoya Peninsula, the northwestern margin of the Costa Rica subduction zone. Because of the advantageous location of the Nicoya Peninsula extending seaward over the seismogenic zone, regional broadband seismic and continuous GPS stations provided unusual instrumental coverage of the megathrust activity over the last decade. Several studies showed that the seismogenic zone below the Nicoya Peninsula is characterized by strong lateral variations in thermal structure (Langseth and Silver, 1996), pore fluids (Audet and Schwartz, 2013; Chaves and Schwartz, 2016), and earthquake behavior (Newman *et al.*, 2002). These variations are largely attributed to differences in genesis of the subducting lithosphere; the northwestern region was generated at the East Pacific Rise (EPR), and the southeastern region was formed at the Cocos–Nazca spreading center (CNS). The position of the EPR–CNS boundary is well defined by magnetic anomalies and high-resolution bathymetry data (Barckhausen *et al.*, 2001). It extends  $\sim 80$  km from the morphological rough–smooth boundary in the older part of the Cocos plate to its orthogonal convergence with the MAT off the central Nicoya Peninsula (Fig. 1).

In addition to hosting large earthquakes every 50–60 yrs, seismic tremor activity and SSEs have been observed every  $\sim 21 \pm 6$  months near transitions between seismic and aseismic slip areas on the megathrust (Dixon *et al.*, 2014). Geodetic observations prior to the 2012 Nicoya earthquake identified a region of slip deficit that tightly encompassed the subsequent rupture area of the event (e.g., Feng *et al.*, 2012). Regions of the plate interface up-dip and down-dip of this stick-slip zone accommodate relative plate motions aseismically, with numerous SSEs being well recorded since 2007. This pattern suggests a partitioning of the plate interface into regions of frictionally stable or unstable sliding behavior.

The extensive regional seismological and geodetic instrumentation available to monitor megathrust activity at close range provides valuable data for studying the partitioning of sliding behavior on the plate boundary below the Nicoya Peninsula through the earthquake cycle. Foreshock activity and a vigorous aftershock sequence were recorded by the local seismic network. The foreshock activity was studied by Walter *et al.* (2015) and found to initiate nine days before the 2012 Nicoya mainshock, plausibly triggered by the regional occurrence of the 27 August 2012  $M_w$  7.3 El Salvador earthquake. This foreshock sequence culminated with a cluster of small-magnitude ( $< 2.2$ ) earthquakes preceding the mainshock by about 35 min and located within 15 km of its hypocenter (Walter *et al.*, 2015). In this article, we focus on the vigorous aftershock sequence and what it contributes to our understanding of the Nicoya megathrust behavior.

## Data and Methods

### Hypocenter Locations

Seismic data used in this study come from stations of the Volcanological and Seismological Observatory of Costa Rica (OVSICORI-UNA) network and the Nicoya Seismic Cycle Observatory (Fig. 1), an international and multiuniversity network of GPS and seismic stations operating on the Nicoya Peninsula, Costa Rica (Dixon *et al.*, 2013). We start with an initial earthquake catalog for the period from the mainshock through the end of 2012 that was generated using the Antelope seismic database automatic earthquake detection and location tools. Subsequently, additional phase arrivals were analyst-picked and reviewed for all events within nine days of the mainshock and for events with  $M \geq 3$  through the end of 2012. The phase information was then used to relocate the events within a local 3D velocity model (DeShon *et al.*, 2006) using the software SIMULPS (Evans *et al.*, 1994), which provides absolute hypocenter locations. Only those earthquakes with the best available locations were retained. We justify focusing our study of the complete aftershock sequence on the first 10 days based on the similarity of the Gutenberg–Richter relationship for this time period versus the four-month period following the mainshock. Both time periods indicate catalog completeness down to  $M_c = 2.2$  and  $b$ -values between 0.80 and 0.85 (Fig. S1, available in the electronic supplement to this article). Because of the deficit in intermediate-to-large magnitude earthquakes that followed the mainshock in 2012, we also determined focal mechanisms for all events with magnitude  $M \geq 4.0$  between 2013 and 2015. Initial hypocenter locations for these events were determined by the OVSICORI-UNA.

### Determination of Earthquake Focal Mechanisms

We apply a regional moment tensor (MT) inversion methodology to determine focal mechanisms for all events in our catalog with magnitude above 4. Second rank general MT inversion is routinely used to obtain source mechanisms of seismic events at teleseismic (e.g., Dziewonski *et al.*, 1981; Ekström *et al.*, 2005) and regional distances (Jost and Herrmann, 1989; Minson and Dreger, 2008). In this study, we adopt the time-domain MT inversion approach (Dreger and Helmberger, 1993), in which the seismic source is simplified by considering a spatial and temporal point source, given by

$$U_n(x, t) = M_{ij} \times G_{ni,j}(x, z, t), \quad (1)$$

in which  $U_n$  is the observed  $n$ th component of displacement,  $M_{ij}$  is the scalar seismic MT, and  $G_{ni,j}$  is the  $n$ th component Green's function for specific force couple orientations. Equation (1) is solved using a least-squares approach for a given source depth. We solve for the deviatoric seismic MT  $M_{ij}$ , which is decomposed into the scalar seismic moment, a double couple (DC) MT (defined by the strike  $[\phi]$ , dip  $[\delta]$ , and

rake  $[\lambda]$  angles of both nodal planes), and a compensated linear vector dipole (CLVD) MT. The MT decomposition is performed following Jost and Herrmann (1989) and is represented as percent DC and CLVD (Fig. 2 and Fig. S2). For each station, three-component waveform data are corrected for instrument response, integrated to displacement and band-pass filtered using a Butterworth filter with corners at 0.02 and 0.05 Hz for events with  $M \geq 4.2$ , and corners at 0.02 and 0.1 Hz for smaller magnitude earthquakes that contain high signal-to-noise ratios. The horizontal traces are rotated to the great circle path to generate tangential and radial components. Green's functions are computed using a frequency–wavenumber integration algorithm (Saikia, 1994) for the 1D local velocity model (DeShon *et al.*, 2006) and filtered similarly to the data. To perform the MT inversion, we assume that epicenter locations represent the actual geographical coordinates of the centroid locations, and the source depth is determined iteratively, finding the solution with the largest variance reduction (VR), defined by

$$VR = \left[ 1 - \frac{\sum_i \sqrt{(\text{data}_i - \text{synth}_i)^2}}{\sqrt{\text{data}_i^2}} \right] \times 100, \quad (2)$$

in which data and synth represent the data and the Green's function time series of the  $i$ th station, respectively. Figure 2 shows an example of the MT process for a large aftershock ( $M_w$  5.5) in the catalog that occurred on 8 September 2012 at 20:29:29 UTC. Figure S2 shows MT results for a much smaller magnitude aftershock ( $M_w$  3.96).

Small events ( $1 \leq M \leq 3.9$ ) represent the majority of the earthquakes in our catalog. Focal mechanisms for small events are commonly determined using  $P$ -wave first-motion polarities (Reasenber and Oppenheimer, 1985). As an improvement on previous algorithms, Hardebeck and Shearer (2002) developed a method for determining first-motion focal mechanisms (the so-called HASH method) that differs from previous techniques in that it accounts for errors in the assumed earthquake locations and seismic-velocity model, as well as in the polarity observations. In this study, we use HASH with manually picked  $P$ -wave polarities from the Antelope seismic database and our improved earthquake locations to determine focal mechanisms for hundreds of small events with magnitudes between 1.5 and 5.4. The HASH method assumes a range in takeoff angles and implements a grid search over all possible focal geometries to identify the acceptable group of solutions for each earthquake. The root mean square deviation between the acceptable nodal planes and the favored nodal plane is the nodal plane uncertainty (Hardebeck and Shearer, 2002; Sumy *et al.*, 2014). The mean of the nodal plane uncertainties represents the focal mechanism quality (e.g., Kilb and Hardebeck, 2006). However, the quality of the focal mechanism for a given event also depends on the number of observations and the azimuthal distribution of these observations over the focal sphere, or the azimuthal gap between stations. If the azimuthal coverage

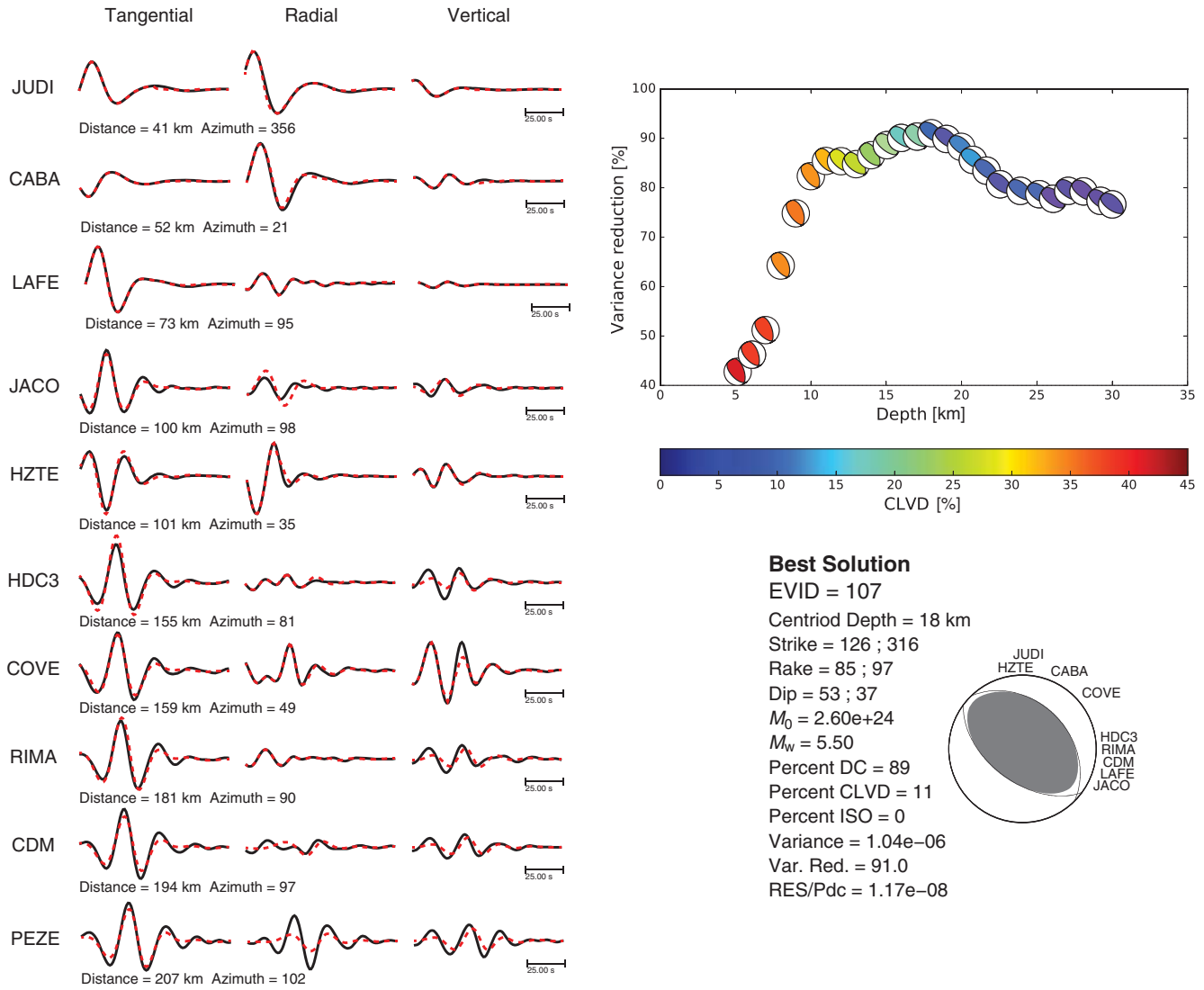


**Figure 2.** Regional moment tensor (MT) inversion of a large aftershock,  $M_w$  5.50, performed using stations from the OVSICORI-UNA network and the Nicoya Seismic Cycle Observatory network. The figure shows the waveform fit between data (continuous lines) and synthetics (dashed lines), the MT decomposition and source parameters. The variance reduction as a function of depth is presented as well. Focal mechanisms are color-coded by compensated linear vector dipole (CLVD) (%).

over the focal sphere is not adequate, determination of the focal geometries will be limited or biased, regardless of the number of stations used in the computation. Thus, we base the quality of the mechanisms (in which A equals best and D equals worst; e.g., Hardebeck and Shearer, 2002) on the mean nodal plane uncertainty and the azimuthal station distribution. In total, we computed 583 earthquake focal mechanisms; 100 using MT inversion and 483 using HASH. These events were relocated using hypoDD (Waldhauser and Ellsworth, 2000) and a recently developed algorithm called GrowClust (Trugman and Shearer, 2017). Both algorithms determine relative earthquake hypocenters using differential travel times obtained from waveform cross correlation of pairs of events observed at a set of common stations (Fig. S3). However, the latter takes an alternative approach to minimize the residuals between the observed

and predicted differential travel times that requires no explicit matrix inversion and optimizes the L1-norm (instead of L2-norm used by hypoDD) of the differential travel-time residuals, improving its robustness to data outliers (Trugman and Shearer, 2017). GrowClust applies a hybrid hierarchical clustering algorithm that simultaneously groups events into clusters based on waveform similarity and relocates each event with respect to its cluster. Furthermore, it implements a nonparametric resampling approach to estimate location uncertainties, allowing an assessment of the relocation results.

Because of its robustness for assessing hypocenter relocations and relative location errors (we found relative horizontal and vertical errors on the order of hundreds of meters), we implement the GrowClust algorithm to produce a final catalog of 347 relative earthquake locations and focal mech-



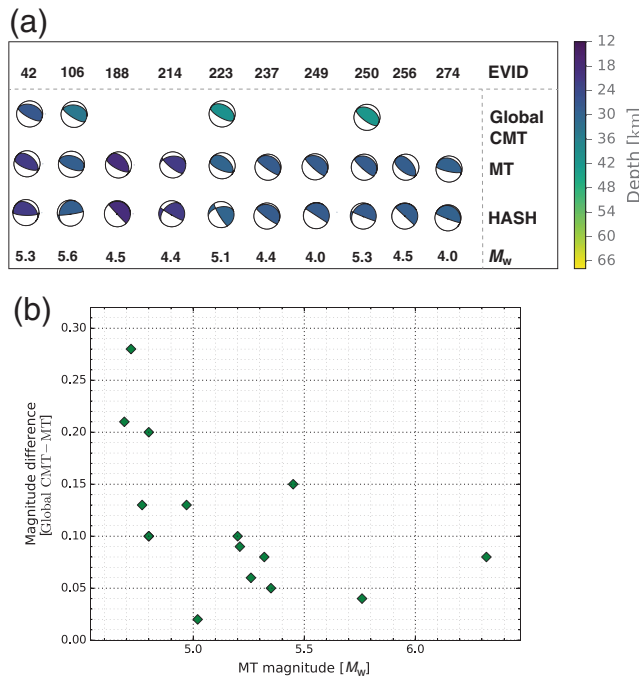


**Figure 3.** Evaluation of focal mechanisms, magnitude, and seismic moment for the 10 largest events in 2012. (a) Focal mechanisms are computed using both methods: The  $P$ -wave first-motion arrivals (HASH method) and the regional MT inversion and compared with the solutions presented in the Global Centroid Moment Tensor (CMT) catalog. Events are organized by ID number (Ⓔ Table S1, available in the electronic supplement to this article),  $M_w$  is from MT, and focal mechanisms are color-coded by depth (km). Note that the solutions from Global CMT and MT sometimes differ substantially from the HASH solution. (b) Estimated  $M_w$  comparison between MT and Global CMT solutions for the largest underthrusting events on the Nicoya Peninsula between the occurrence of the 2012 earthquake and the end of 2015.

anisms. We selected only those events with quality A and B focal mechanisms for this subset. This catalog is listed in Ⓔ Table S1. A comparison of epicentral locations for these 347 events determined using both relocation methods is shown in Ⓔ Figure S3 along with a close-up window exhibiting the clustering of events produced with the GrowClust algorithm. In general, both techniques result in very similar locations, with GrowClust providing superior error estimates. HASH assumes uncertainties in earthquake location, velocity structure, and first-motion polarity assessment in its determination of the best focal mechanism. Therefore, the small differences in azimuth and takeoff angle that result from relocation using hypoDD or GrowClust do not require us to recompute faulting geometries after earthquake relocation. Twenty-one of these relocated events are reported in the Global Centroid Moment Tensor (CMT) catalog. Figure 3 compares the focal mechanism solutions and magnitudes obtained using the MT, HASH, and Global CMT methods for the largest events in our catalog that have multiple solutions determined. In general, the agreement between faulting geometries and  $M_w$  is quite robust (although it is well known

Table 1

Focal Mechanism Orientation Selection Criteria for Underthrusting Events

	Nodal Plane	Strike (°)	Dip (°)	Rake (°)
Mainshock	1	308	17	102
	2	115	73	86
Selection criteria	1	260–350	<40	35–135
	2	75–145	>50	35–135

that the precision of moment magnitude estimates decreases for events with  $M_w \leq 5.0$ ). For events with multiple focal mechanism solutions, we use the MT solution. Because much of the following analysis relies on events located on the plate interface, we identify these events based on their location being near (within 8 km) the previously defined plate interface (DeShon *et al.*, 2006) and having nodal planes consistent with the mainshock (a total of 210 events). Depth estimates have uncertainties, and because we view it as unlikely that there are many thrust events on shallower or deeper planes parallel to the megathrust, we consider mechanism information more reliable than depth in identifying events located on the plate interface. We therefore use a generous 8-km distance range from the megathrust together with focal mechanism constraints to define events occurring on the plate interface. The range of thrust-faulting geometries we consider consistent with the mainshock is indicated in Table 1. In the following, we refer to these 210 events as interface thrust aftershocks.

## Results and Discussion

The locations of 347 relocated earthquakes with computed focal mechanisms, ranging in magnitude between 1.5 and 6.4, are shown in Figure 4. Almost all of the events are located either within the downgoing slab or on the plate interface. We interpret most of the events as occurring on the thrust interface located up-dip of the peak coseismic slip and at the southern margin of the peninsula (Fig. 5), where coseismic rupture also reached more than 1 m of slip (Yue *et al.*, 2013; Protti *et al.*, 2014; Liu *et al.*, 2015). Many of the events up-dip of the peak coseismic slip occur in the offshore slip-deficit patch identified with GPS and Interferometric Synthetic Aperture Radar (Feng *et al.*, 2012; Xue *et al.*, 2015) that failed to slip during the mainshock (Protti *et al.*, 2014). Aftershock sequences observed for the 2005  $M_w$  8.7 Nias-Simeulue, Sumatra, earthquake (Hsu *et al.*, 2006), the 2010  $M_w$  8.8 Maule earthquake (Rietbrock *et al.*, 2012), and the 2011  $M_w$  9.0 Tohoku-Oki megathrust (Asano *et al.*, 2011) show a preponderance of events that rupture in areas surrounding the main coseismic slip asperity, either at transitions from high- to low-slip or in low-slip regions, with fewer and small magnitude events locating within the maximum coseismic slip area. Similarly, Ito *et al.* (2004) showed that aftershocks of the 2003  $M_w$  8.0 Tokachi-Oki earthquake exhibited a spatial distribution that localized off the main

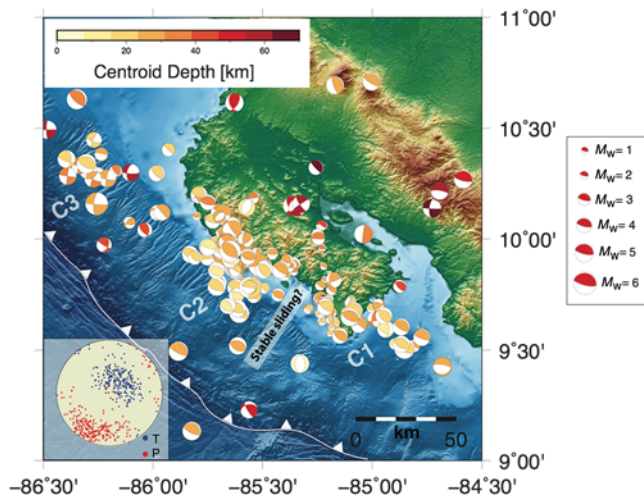


**Figure 4.** Map showing the spatial distribution of all well-located aftershocks with focal mechanisms computed for the 5 September 2012 Nicoya Peninsula, Costa Rica, earthquake sequence. The pressure (P) and tension axes (T) diagram is embedded within the figure. Focal mechanisms are color-coded by centroid depth. The size of the mechanism corresponds with the magnitude of each event. Note the clustering (groups: C1, C2, and C3) and segmentation of the plate interface, as discussed in the text.

coseismic slip patch, northwest from the epicenter. For large megathrust earthquakes, it is widely accepted that the mainshock releases a large fraction of the strain accumulated during the interseismic cycle. Aftershock seismicity, especially the largest events, should therefore be predominantly located in areas of transition between high and low slips or on the margins of high-slip regions where the Coulomb static stresses increased due to the sudden slip during the main event. Nicoya interplate aftershocks also appear to be sandwiched between regions of large coseismic slip (down-dip) and slow slip (up-dip) in the northwest or between two patches of slow slip in the southeast (Fig. 5), confirming a previous suggestion that the Nicoya plate interface may have a sharp along-dip transition in frictional properties from velocity weakening at depth to velocity strengthening or conditionally stable at shallow depth (Walter *et al.*, 2013).

The aftershocks with thrusting mechanisms occur in two dominant spatial clusters (clusters C1 and C2 in Figs. 4 and 5), whereas there is a third spatial cluster with predominantly strike-slip mechanisms located offshore to the northwest (cluster C3 in Fig. 4). The lack of activity between C1 and C2 might be due to the lack of coseismic slip in this region or a possible change in the frictional properties of the plate interface. This gap in aftershock activity correlates with a shallowing of the plate interface in a recently proposed model (Kyriakopoulos *et al.*, 2015). If the plate interface experiences different physical conditions in this region because of its distorted geometry, it might also have a different mode of slip, with stable sliding rather than stick-slip motion. This interpretation is supported by the work of Wang and Bilek (2011), who suggested that subducted topographic highs

might result in stable sliding due to preferential release of fluid and a reduction in the effective normal stress.

Cross sections of the low-angle thrust-faulting events within seismicity clusters C1 and C2 are consistent with previous observations that show a change in the depth of plate interface events across the EPR–CNS plate suture (Protti *et al.*, 1994; Newman *et al.*, 2002; Hansen, 2006). In the northern part of the peninsula (cluster C2), most of the underthrusting events are in the depth range between 18 and 30 km. To the south (cluster C1 in Fig. 5), underthrusting events show an  $\sim 5$  km reduction in depth, with most events locating between 13 and 25 km in depth. This variability in the depth of interplate seismicity has been linked to the difference in the thermal structure of subducted lithosphere associated with different genesis; colder EPR (deeper seismicity) subducting to the north and warmer CNS (shallower seismicity) in the south (Langseth and Silver, 1996).

All Nicoya aftershock thrust events locate at depths between 10 and 32 km, with a peak in the kernel density estimation (KDE) function at 20 km (Fig. 6). Hypocenters determined using the same velocity model for underthrusting events that occurred before the mainshock have a similar distribution of depths (DeShon *et al.*, 2006; Hansen, 2006), spanning from 10 to  $\sim 30$  km, with a peak in the KDE at 18 km (Fig. 6). Coseismic slip during the Nicoya Peninsula earthquake spanned a larger depth range of the plate interface, with slip distributed between  $\sim 5$  and 35 km, but large slip concentrated below 20 km (Fig. 6). These depth profiles of earthquake behavior during the interseismic, coseismic, and postseismic stages of the earthquake cycle suggest the following about the mechanical behavior of the plate interface: (1) the seismogenic zone, where earthquakes can nucleate, extends from  $\sim 10$  to 32 km; (2) the lower few kilometers of this region were completely locked during the late interseismic stage such that no underthrusting events occurred in this depth range prior to the mainshock but aftershocks did rupture this depth range; and (3) the mainshock rupture extended into conditionally stable parts of the plate interface both up-dip and down-dip of the seismogenic zone (Fig. 6). Large SSEs accompanied by tremor occurred repeatedly at both shallow (0–10 km) and deep (30–50 km) depths in this region (Dixon *et al.*, 2014) and fit well with this depth variation along the plate interface.

In addition to the interplate events, focal mechanisms were computed for a number of  $M \geq 4$  aftershocks that locate at depth within the subducting lithosphere offshore the northwest margin of the Nicoya Peninsula between 20 and 35 km in depth (cluster C3 in Fig. 4). The majority of the events in this cluster C3 have nearly pure strike-slip mechanisms with shallow-plunging northeast–southwest-oriented pressure axes, consistent with the orientation of the regional maximum compressive stress direction. Local seismicity catalogs created for specific periods of time in 1999, 2007, and 2009 also contain a large number of events at this same location, demonstrating that this activity is persistent and not simply related to the occurrence of the mainshock (e.g., clusters

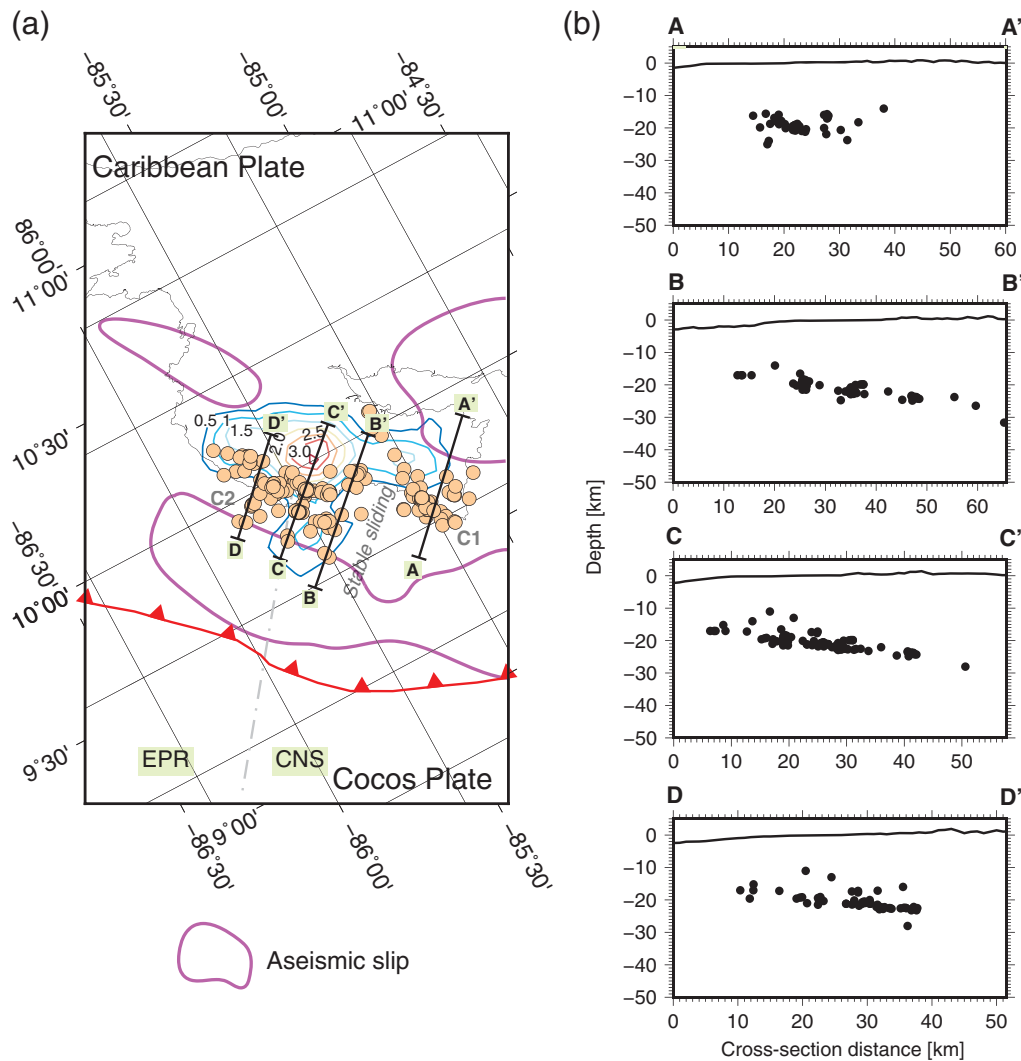


**Figure 5.** (a) Spatial distribution of underthrusting events that followed the 5 September 2012, Nicoya Peninsula, Costa Rica, earthquake. Underthrusting events are identified by their location relative to the plate interface and their focal mechanisms. The colored contours in the central and southern margins of the Peninsula represent the coseismic rupture area of the mainshock (slip increments of 0.5 m; Liu *et al.*, 2015). The magenta contours up-dip and down-dip highlight the regions of accumulated slow slip between 2007 and 2012 (Dixon *et al.*, 2014). Cross section D–D' shows the distribution of events located north of the EPR–CNS boundary. Note the difference in depth extension along strike.

OC1 and OC2 in (E) Fig. S4). Because subduction of the oceanic lithosphere is at an oblique angle to the trench, internal deformation (contortions) of the downgoing plate during the subduction process could explain the occurrence of these events (e.g., Pacheco and Singh, 2010).

Although the large majority of low-angle thrust focal mechanisms observed in this study are consistent with the regional stress orientation given by the principal pressure (P) and tension (T) axes (here, we consider the average directions of the P and T axes to be indicators of the general orientations of the maximum compressive stress  $\sigma_1$  and the least compressive stress  $\sigma_3$ ), and the slip history on the megathrust (Yue *et al.*, 2013; Protti *et al.*, 2014; Liu *et al.*, 2015), a diversity in fault geometries with respect to the mainshock focal mechanism is observed. These deviations are possibly linked to Coulomb static stress changes (earthquake interaction) imposed by the mainshock, earthquake afterslip

(Malservisi *et al.*, 2015), spatial heterogeneities along the plate interface (Fagereng and Sibson, 2010), or possibly a combination of all of these.

### Coulomb Static Stress Change Effects

It has been demonstrated that large earthquake ruptures permanently deform the surrounding medium, changing the stress conditions of nearby crustal materials as a function of their location, geometry, and sense of slip (Toda, Lin, *et al.*, 2011). Unlike dynamic stress (an oscillatory wavefield that can trigger earthquakes both near to and far from the source), earthquake interaction through the static stress field can result in both an increase in seismicity in areas of coseismic static stress and seismic quiescence in stress shadow areas (Harris and Simpson, 1996). The brittle failure of faults is thought to be a result of the combination of the effective

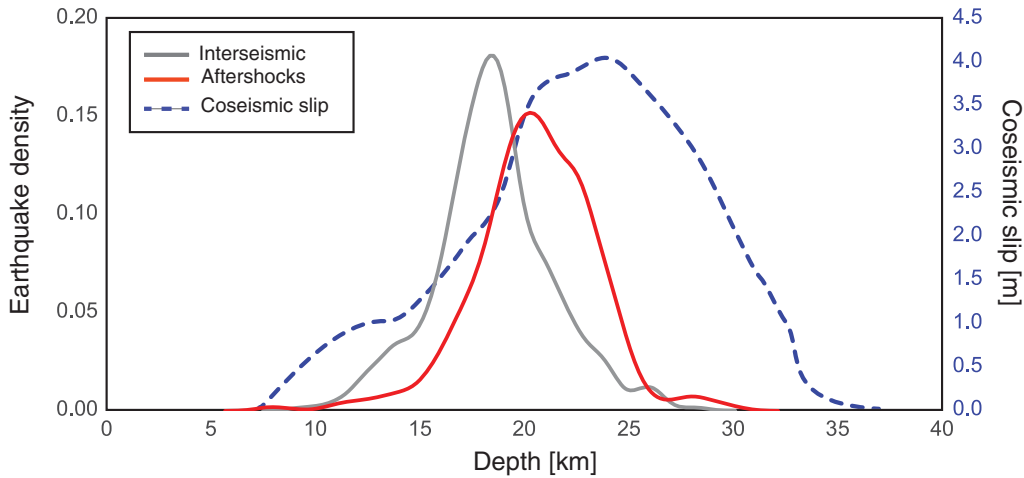


**Figure 6.** Kernel density estimate functions for the depth distribution of underthrusting events during the interseismic period (DeShon *et al.*, 2006) and the aftershock sequence of the 2012 Nicoya Peninsula earthquake (continuous line) plotted with the coseismic slip (m) generated by the mainshock (dashed line).

normal and shear stress conditions, commonly quantified as the Coulomb failure criterion (e.g., King *et al.*, 1994; Scholz, 2002), defined as

$$\Delta\text{CFS} = \Delta\tau + \mu'(\Delta\sigma), \quad (3)$$

in which  $\tau$  is the shear stress on the fault plane (positive in the inferred direction of slip),  $\sigma$  is the normal stress (positive for unclamping), CFS is Coulomb failure stress, and  $\mu'$  is the apparent coefficient of friction. Failure is promoted if  $\Delta\text{CFS}$  is positive and inhibited if negative. The location, geometry, and slip distribution of the earthquake rupture as well as the friction coefficient play an important role in the calculation of the  $\Delta\text{CFS}$  produced by an earthquake. Previous work (e.g., King *et al.*, 1994; Hardebeck *et al.*, 1998; Stein, 1999) demonstrated that an increase or decrease in the Coulomb static stresses off the causative fault of less than 1 bar (0.1 MPa) is sufficient to promote either earthquake failure or seismic quiescence, respectively. Because of its apparent role in triggering or halting of aftershocks and subsequent mainshocks on nearby faults (within a distance proportional to a few fault dimensions), Coulomb static stress changes have been proposed as a basis for evaluating short-term earthquake hazards in multiple tectonic environments.

The Coulomb static stress change induced by the 2012 Nicoya earthquake was computed on the plate interface using the coseismic slip model of Liu *et al.* (2015), combined with the contribution of the first 3-hr afterslip deformation (Malservisi *et al.*, 2015) following the approach of Toda, Stein, Lin, and Sevilgen (2011). We assumed a homogeneous elastic half-space and a common choice for the friction coefficient of 0.4. (It has been proven difficult to discriminate among possible values of friction coefficient in Coulomb static friction studies, and a midvalue of 0.4 is commonly adopted. We consider a range from 0.2 to 0.8, and 0.4 actually optimizes the consistency of predicted Coulomb stress changes and aftershock occurrence for our data, but it does

not necessarily reflect the strength of the megathrust.) The overall spatial distribution of most of the larger underthrusting events up-dip of the area of maximum coseismic slip and at the southeastern margin of the Peninsula (clusters C1 and C2 in Figs. 4 and 5) is well explained by regions of static stress increase on the megathrust plane induced by the mainshock (Fig. 7). Little aftershock activity occurs down-dip, suggesting that the deep coseismic slip released almost all of the accumulated elastic strain in the deeper part of the seismogenic zone, leaving none sufficient to result in brittle failure. Nonetheless, about 20% of smaller magnitude underthrusting events are located in areas of transition between positive and negative static stress changes or in regions of reduced driving stress, suggesting that other mechanisms such as dynamic perturbation of fluid conditions or postseismic creep of the fault (Malservisi *et al.*, 2015) may be responsible for triggering some of the interplate earthquakes.

Although it is not unexpected for a large percentage of aftershocks on the mainshock fault plane to locate in regions of calculated Coulomb stress increase (e.g., King *et al.*, 1994), a more stringent test of the Coulomb stress-triggering hypothesis is whether the fault planes of all aftershocks throughout the source region are suitably oriented for failure to have been promoted by the mainshock slip (consistent with the  $\Delta\text{CFS}$  hypothesis). Resolving the Coulomb stress change on the nodal planes (rake directions) of aftershock sequences requires no assumptions about the regional stress field but does depend on the mainshock source rupture model and the assumed coefficient of friction (King *et al.*, 1994; Toda, Lin, *et al.*, 2011; Toda, Stein, and Lin, 2011). Although shear stresses are similar for both nodal planes, the normal stress is different (Hardebeck *et al.*, 1998), and thus,  $\Delta\text{CFS}$  varies for the orthogonal planes.

We tested the Coulomb static-stress-triggering hypothesis on just the interface-aligned nodal plane for the catalog of underthrusting aftershock focal mechanisms (Table 1) and



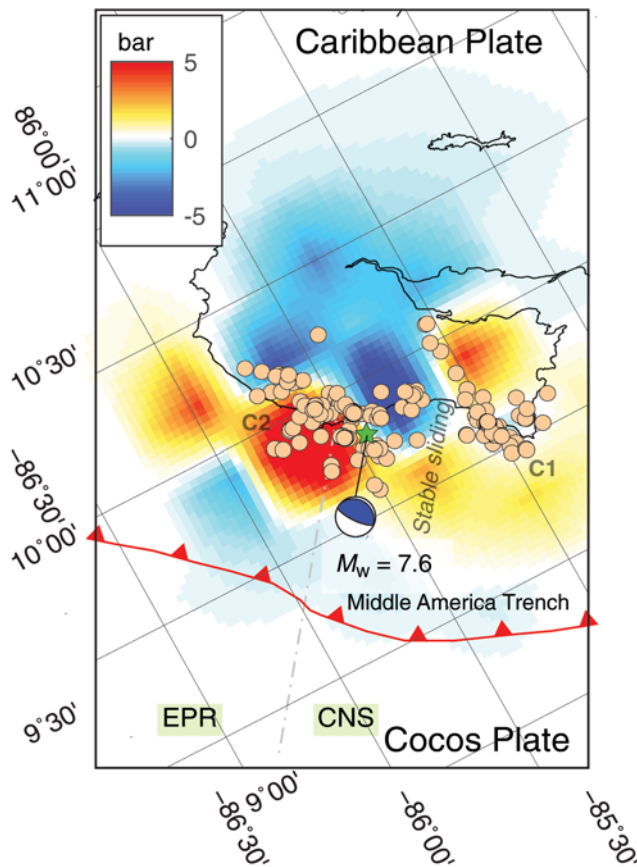


**Figure 7.** Map view of the Coulomb failure stress (CFS) on the plate interface induced by the 2012  $M_w$  7.6 Nicoya Peninsula, Costa Rica, earthquake. The CFS was computed using the slip model of Liu *et al.* (2015) and the 3-hr afterslip model of Malservisi *et al.* (2015), assuming an optimal receiver fault with geometry (strike: 308; dip 17; slip vector 102). The hypocenter of the mainshock (green star) is located at 13 km depth. Circles locate underthrusting events identified by the selection criteria discussed in the text.

on both nodal planes for the remaining events (Fig. 8). We examined the effect of the friction coefficient using four values (0.2, 0.4, 0.6, and 0.8) and found that 0.4 is the value that produces the greatest number of events with positive Coulomb static stress change, as has been observed in previous studies (Toda, Lin, *et al.*, 2011). Figure 8b shows the distribution of events with positive and negative  $\Delta CFS$  as a function of friction coefficient. For a friction coefficient of 0.4, we found that 80% of the aftershocks experience positive Coulomb stress change that would promote its failure, and 20% of the aftershocks show negative Coulomb stress change that would inhibit their failure. In some regions, variable mechanisms with both positive and negative Coulomb stress changes are spatially intermingled. Similar analyses (Hardebeck *et al.*, 1998; Sato *et al.*, 2013; Sumy *et al.*, 2014; Zhu and Miao, 2015) showed that focal mechanisms with both positive and negative Coulomb static stress changes are spatially intermingled, even though nearby aftershocks may have quite similar fault geometries. Thus, although many of the focal mechanisms exhibit similar geometry to that of the main-

shock, small rotations in the receiver fault geometry and/or uncertainties in the coseismic and afterslip models can significantly affect the Coulomb stress calculation.

Figure 9 shows the location of underthrusting aftershocks with positive and negative Coulomb stress changes together with the 70-day afterslip distribution (Malservisi *et al.*, 2015). Most of the aftershocks occur in regions of enhanced afterslip (at least 0.3 m). Therefore, the distribution of underthrusting aftershocks can be explained by either the static stress change induced by the mainshock or by accelerated fault creep during afterslip, or both. Of course, there are many uncertainties in the mainshock slip distribution, the precise megathrust geometry, the faulting mechanisms of the aftershocks, the locations of the aftershocks, and in the lack of specific knowledge of prestress in the region prior to the mainshock (Feng *et al.*, 2012), so we do not want to overinterpret the 80% consistency found here, other than as a compatibility result for reasonable elastic stress transfer effects.

Most of the observations bearing on the mechanical behavior of the plate interface are summarized in Figure 9. We infer that the region accumulating strain prior to the Nicoya mainshock (dark contour) spanned the entire seismogenic zone ( $\sim 10$ – $32$  km in depth) and experienced the maximum coseismic slip or afterslip in the down-dip and up-dip parts of the locked patch, respectively. The large majority of the underthrusting aftershocks (circles) occurred up-dip of maximum coseismic slip in regions of large afterslip. Portions of the plate interface that failed in slow slip locate both up-dip and down-dip of the seismogenic zone. Although no aftershocks occur in the slow-slip regions, some mainshock slip likely extended into these zones.

## Conclusions

We examine the aftershock sequence of the 5 September 2012  $M_w$  7.6 Nicoya Peninsula, Costa Rica, earthquake in terms of hypocenter locations and fault geometries. Focal mechanisms for the larger magnitude events are generated using full waveform MT inversions. We use  $P$ -wave first-motion polarities to determine the faulting geometries of the smaller magnitude earthquakes. Coulomb static stress changes on the plate interface and on the nodal planes of the aftershocks induced by the mainshock slip and first three days of afterslip are computed and compared with the spatial distribution of afterslip.

We find that underthrusting aftershocks span the depth range 12–32 km but are concentrated up-dip, adjacent to the main coseismic slip and at the southernmost edge of the Nicoya Peninsula, defining two discrete patches that are separated by a conspicuous gap in aftershock activity. This gap might be due to the lack of coseismic slip in this region or might represent an along-strike variation in the frictional behavior of the plate interface that relates to the morphology of the subducted slab. Interface seismicity during the interseismic cycle is constrained to shallower depths on the plate interface (12–25 km). The coseismic slip extends several

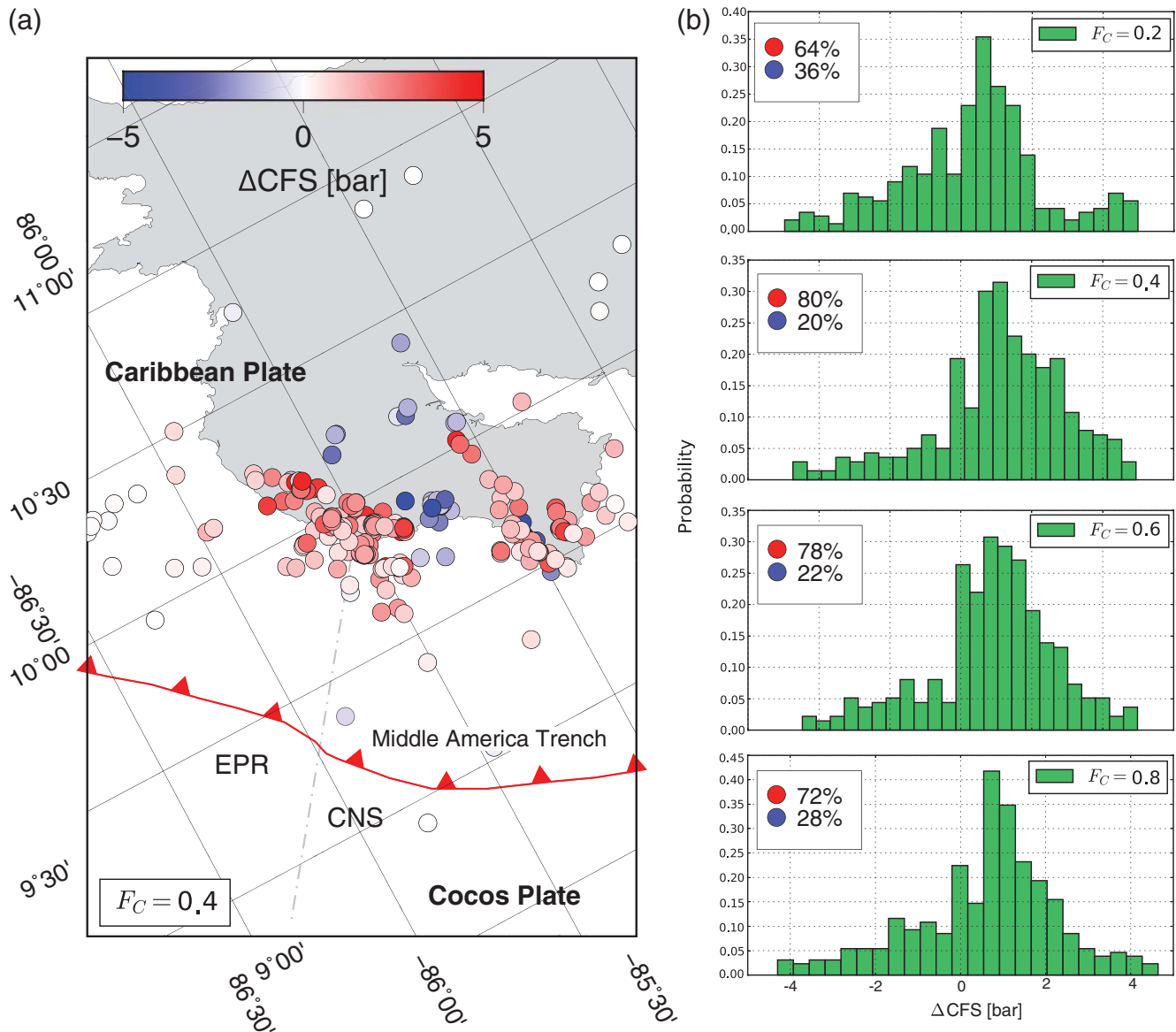


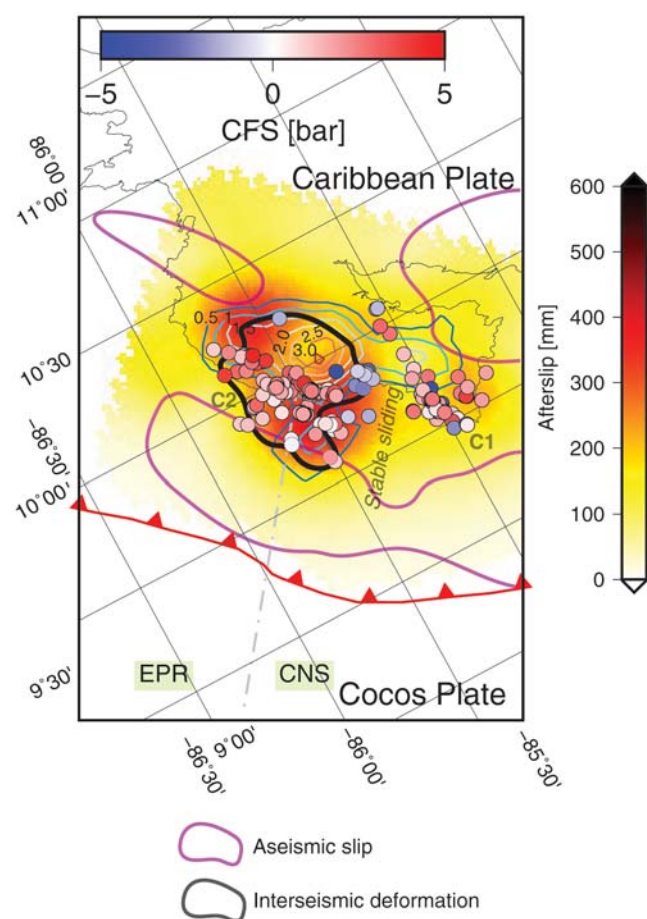
**Figure 8.** (a) The Coulomb static stress change computed on the nodal planes of the entire catalog of aftershocks analyzed in this study. Positive circles (80%) are events with mechanisms in which one or both nodal planes correspond positively with the Coulomb static stress hypothesis. Negative circles (20%) represent seismicity that is not triggered by the Coulomb static stress change induced by the mainshock (neither nodal plane is favored for failure). (b) Histograms showing the distribution of positive and negative CFS on the nodal plane of the aftershocks as a function of friction coefficient.

kilometers up-dip and down-dip of the interplate aftershocks into regions of the plate interface that exhibit slow slip. This pattern suggests that the mainshock ruptured a strongly locked patch driving down-dip slip into a normally velocity-strengthening part of the deep plate interface that hosts SSEs. Our observations suggest that large earthquakes can rupture into areas that may be aseismic normally, indicating conditionally stable frictional behavior. A total of  $\sim 20\%$  of the underthrusting aftershocks are located in regions that are unsuitable for failure induced by the mainshock slip and the 3-hr afterslip (correlate negatively with the Coulomb static-stress-triggering hypothesis). The locations of these events do agree well with the 70-day afterslip pattern, indicating that

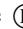
the aftershock distribution can be explained by a combination of afterslip and static stress changes following the mainshock. It is likely that these are related, with afterslip being the response of the plate interface away from the main stick-slip asperity to the increased static stress resulting from coseismic slip, with aftershocks being local responses to this afterslip.

### Data and Resources

All seismic data from the Nicoya Seismic Cycle Observatory are available at the Incorporated Research Institutions for Seismology Data Management Center (IRIS DMC; <http://ds.iris.edu/ds/nodes/dmc/>, last accessed in August 2016). All



**Figure 9.** Map showing afterslip associated with the intermediate relaxation time (70 days) documented in Malservisi *et al.* (2015). Light contours represent the coseismic slip area of the 2012  $M_w$  7.6 Nicoya mainshock from Liu *et al.* (2015), and the dark contour outlines the region of strain accumulation from Feng *et al.* (2012). The cumulative slip of 1 m from slow-slip events (SSEs) is represented by the up-dip and down-dip magenta curves (Dixon *et al.*, 2014). Circles represent aftershocks located along the plate interface. Eighty percent of the underthrusting events correspond positively with the Coulomb static stress change induced by the occurrence of the Nicoya Peninsula earthquake, assuming the interplate fault-plane choice. These events all locate within regions of intermediate-to-high afterslip.

data needed to reach the conclusions in the article are present in the article and/or in the  electronic supplement to this article. Additional data related to this article may be requested from the authors. Antelope seismic database software is available at [www.brrt.com](http://www.brrt.com) (last accessed in August 2016). Figures were generated using the free seismological community scientific library ObsPy (e.g., Beyreuther *et al.*, 2010).

### Acknowledgments

We thank M. Protti and V. González from Observatorio Vulcanológico y Sismológico de Costa Rica Universidad Nacional (OVSICORI-UNA) for installing and operating the Nicoya seismic network with critical support from A. Newman and D. Sampson. Associate Editor Tom Brocher and two anonymous reviewers provided very helpful suggestions to improve the article. This work was supported by the National Science Foundation

(NSF) under Grant Number EAR-1321550 to S. Y. S. and by a Continuously Operating Caribbean Global Positioning System (GPS) Observational Network (UNAVCO COCONet) Fellowship to E. J. C. and T. Lay that is supported by NSF Grant EAR1245717. E. J. C. acknowledges support from UNA and Consejo Nacional para Investigaciones Científicas y Tecnológicas de Costa Rica (CONICIT).

### References

- Asano, Y., T. Saito, Y. Ito, K. Shiomi, H. Hirose, T. Matsumoto, S. Aoi, S. Hori, and S. Sekiguchi (2011). Spatial distribution and focal mechanisms of aftershocks of the 2011 off the Pacific coast of Tohoku earthquake, *Earth Planets Space* **63**, no. 7, 669–673, doi: [10.5047/eps.2011.06.016](https://doi.org/10.5047/eps.2011.06.016).
- Audet, P., and S. Y. Schwartz (2013). Hydrologic control of forearc strength and seismicity in the Costa Rican subduction zone, *Nature Geosci.* **6**, no. 10, 852–855, doi: [10.1038/ngeo1927](https://doi.org/10.1038/ngeo1927).
- Barckhausen, U., C. R. Ranero, R. von Huene, S. C. Cande, and H. A. Roeser (2001). Revised tectonic boundaries in the Cocos Plate off Costa Rica: Implications for the segmentation of the convergent margin and for plate tectonic models, *J. Geophys. Res.* **106**, no. B9, 19207–19220, doi: [10.1029/2001JB000238](https://doi.org/10.1029/2001JB000238).
- Beyreuther, M., R. Barsch, L. Krischer, T. Megies, Y. Behr, and J. Wassermann (2010). ObsPy: A Python toolbox for seismology, *Seismol. Res. Lett.* **81**, no. 3, 530–533, doi: [10.1785/gssrl.81.3.530](https://doi.org/10.1785/gssrl.81.3.530).
- Chaves, J. E., and S. Y. Schwartz (2016). Monitoring transient changes within overpressured regions of subduction zones using ambient seismic noise, *Sci. Adv.* **2**, no. 1, doi: [10.1126/sciadv.1501289](https://doi.org/10.1126/sciadv.1501289).
- DeMets, C., R. G. Gordon, and D. F. Argus (2010). Geologically current plate motions, *Geophys. J. Int.* **181**, 1–80, doi: [10.1111/j.1365-246X.2009.04491.x](https://doi.org/10.1111/j.1365-246X.2009.04491.x).
- DeShon, H. R., S. Y. Schwartz, A. V. Newman, V. Gonzalez, M. Protti, L. M. Dorman, T. H. Dixon, D. E. Sampson, and E. R. Flueh (2006). Seismogenic zone structure beneath the Nicoya Peninsula, Costa Rica, from three-dimensional local earthquake  $P$ - and  $S$ -wave tomography, *Geophys. J. Int.* **164**, no. 1, 109–124, doi: [10.1111/j.1365-246X.2005.02809.x](https://doi.org/10.1111/j.1365-246X.2005.02809.x).
- Dixon, T. H., Y. Jiang, R. Malservisi, R. McCaffrey, N. Voss, M. Protti, and V. Gonzalez (2014). Earthquake and tsunami forecasts: Relation of slow slip events to subsequent earthquake rupture, *Proc. Natl. Acad. Sci. Unit. States Am.* **111**, no. 48, 17,039–17,044, doi: [10.1073/pnas.1412299111](https://doi.org/10.1073/pnas.1412299111).
- Dixon, T. H., S. Y. Schwartz, M. Protti, V. Gonzalez, A. Newman, J. Marshall, and J. Spotila (2013). Detailed data available for recent Costa Rica earthquake, *Eos Trans. AGU* **94**, 17–18.
- Dreger, D. S., and D. V. Helmberger (1993). Determination of source parameters at regional distances with three-component sparse network data, *J. Geophys. Res.* **98**, no. B5, 8107–8125, doi: [10.1029/93JB00023](https://doi.org/10.1029/93JB00023).
- Dziewonski, A. M., T. A. Chou, and J. H. Woodhouse (1981). Determination of earthquake source parameters from waveform data for studies of global and regional seismicity, *J. Geophys. Res.* **86**, no. B4, 2825–2852, doi: [10.1029/93JB00023](https://doi.org/10.1029/93JB00023).
- Ekström, G., A. M. Dziewonski, and N. N. Maternovskaya (2005). Global seismicity of 2003: Centroid-moment-tensor solutions for 1087 earthquakes, *Phys. Earth Planet. In.* **148**, nos. 2/4, 327–351, doi: [10.1016/j.pepi.2004.09.006](https://doi.org/10.1016/j.pepi.2004.09.006).
- Evans, J. R., D. Eberhart-Phillips, and C. H. Thurber (1994). User's manual for SIMULPS12 for imaging  $V_P$  and  $V_P/V_S$ : A derivative of the Thurber tomographic inversion SIMUL3 for local earthquakes and explosions, *U.S. Geol. Surv. Open-File Rept.* 94-431, U.S. Government Printing Office.
- Fagereng, A., and R. H. Sibson (2010). Melange rheology and seismic style, *Geology* **38**, no. 8, 751–754, doi: [10.1130/G30868.1](https://doi.org/10.1130/G30868.1).
- Feng, L., A. V. Newman, M. Protti, V. Gonzalez, Y. Jiang, and T. H. Dixon (2012). Active deformation near the Nicoya Peninsula, northwestern Costa Rica, between 1996 and 2010: Interseismic megathrust coupling, *J. Geophys. Res.* **117**, no. B6, doi: [10.1029/2012JB009230](https://doi.org/10.1029/2012JB009230).



- Hansen, S. E. (2006). Earthquake relocation and focal mechanism determination using waveform cross correlation, Nicoya Peninsula, Costa Rica, *Bull. Seismol. Soc. Am.* **96**, no. 3, 1003–1011, doi: [10.1785/0120050129](https://doi.org/10.1785/0120050129).
- Hardebeck, J. L., and P. M. Shearer (2002). A new method for determining first-motion focal mechanisms, *Bull. Seismol. Soc. Am.* **92**, no. 6, 2264, doi: [10.1785/0120010200](https://doi.org/10.1785/0120010200).
- Hardebeck, J. L., J. J. Nazareth, and E. Hauksson (1998). The static stress change triggering model: Constraints from two southern California aftershock sequences, *J. Geophys. Res.* **103**, no. B10, 24,427–24,437, doi: [10.1029/98JB00573](https://doi.org/10.1029/98JB00573).
- Harris, R. A., and R. W. Simpson (1996). In the shadow of 1857—The effect of the Great Ft. Tejon earthquake on subsequent earthquakes in southern California, *Geophys. Res. Lett.* **23**, no. 3, 229–232, doi: [10.1029/96GL00015](https://doi.org/10.1029/96GL00015).
- Hsu, Y. J., M. Simons, J. P. Avouac, and J. Galetzka (2006). Frictional after-slip following the 2005 Nias-Simeulue earthquake, Sumatra, *Science* **312**, 1921, doi: [10.1126/science.1126960](https://doi.org/10.1126/science.1126960).
- Ito, Y., H. Matsubayashi, H. Kimura, T. Matsumoto, Y. Asano, and S. Sekiguchi (2004). Spatial distribution for moment tensor solutions of the 2003 Tokachi-oki earthquake ( $M_{JMA} = 8.0$ ) and aftershocks, *Earth Planets Space* **56**, no. 3, 301–306, doi: [10.1186/BF03353055](https://doi.org/10.1186/BF03353055).
- Jost, M. L., and R. B. Herrmann (1989). A student's guide to and review of moment tensors, *Seismol. Res. Lett.* **60**, no. 2, 37–57.
- Kilb, D., and J. L. Hardebeck (2006). Fault parameter constraints using relocated earthquakes: A validation of first-motion focal-mechanism data, *Bull. Seismol. Soc. Am.* **96**, no. 3, 1140–1158, doi: [10.1785/0120040239](https://doi.org/10.1785/0120040239).
- King, G. C. P., R. S. Stein, and J. Lin (1994). Static stress changes and the triggering of earthquakes, *Bull. Seismol. Soc. Am.* **84**, no. 3, 935–953.
- Kyriakopoulos, C., and A. V. Newman (2016). Structural asperity focusing locking and earthquake slip along the Nicoya megathrust, Costa Rica, *J. Geophys. Res.* **121**, 5461–5476, doi: [10.1002/2016JB012886](https://doi.org/10.1002/2016JB012886).
- Kyriakopoulos, C., A. V. Newman, A. M. Thomas, M. Moore-Driskell, and G. T. Farmer (2015). A new seismically constrained subduction interface model for Central America, *J. Geophys. Res.* **120**, no. 8, 5535–5548, doi: [10.1002/2014JB011859](https://doi.org/10.1002/2014JB011859).
- Langseth, M. G., and E. A. Silver (1996). The Nicoya convergent margin—A region of exceptionally low heat flow, *Geophys. Res. Lett.* **23**, no. 8, 891–894.
- Liu, C., Y. Zheng, X. Xiong, R. Wang, A. López, and J. Li (2015). Rupture processes of the 2012 September 5  $M_w$  7.6 Nicoya, Costa Rica earthquake constrained by improved geodetic and seismological observations, *Geophys. J. Int.* **203**, no. 1, 175–183, doi: [10.1093/gji/ggv295](https://doi.org/10.1093/gji/ggv295).
- Malservisi, R., S. Y. Schwartz, N. Voss, M. Protti, V. Gonzalez, T. H. Dixon, Y. Jiang, A. V. Newman, J. Richardson, J. I. Walter, and D. Vayenko (2015). Multiscale postseismic behavior on a megathrust: The 2012 Nicoya earthquake, Costa Rica, *Geochem. Geophys. Geosys.* **16**, no. 6, 1848–1864, doi: [10.1002/2015GC005794](https://doi.org/10.1002/2015GC005794).
- Minson, S. E., and D. S. Dreger (2008). Stable inversions for complete moment tensors, *Geophys. J. Int.* **174**, no. 2, 585–592, doi: [10.1111/j.1365-246X.2008.03797.x](https://doi.org/10.1111/j.1365-246X.2008.03797.x).
- Newman, A. V., S. Y. Schwartz, V. Gonzalez, H. R. DeShon, J. M. Protti, and L. M. Dorman (2002). Along strike variability in the seismogenic zone below Nicoya Peninsula, Costa Rica, *Geophys. Res. Lett.* **29**, no. 20, 38-1–38-4, doi: [10.1029/2002GL015409](https://doi.org/10.1029/2002GL015409).
- Pacheco, J. F., and S. K. Singh (2010). Seismicity and state of stress in Guerrero segment of the Mexican subduction zone, *J. Geophys. Res.* **115**, no. B01303, doi: [10.1029/2009JB006453](https://doi.org/10.1029/2009JB006453).
- Protti, M., V. Gonzalez, A. V. Newman, T. H. Dixon, S. Y. Schwartz, J. S. Marshall, L. Feng, J. I. Walter, R. Malservisi, and S. E. Owen (2014). Nicoya earthquake rupture anticipated by geodetic measurement of the locked plate interface, *Nature* **7**, no. 2, 117–121, doi: [10.1038/ngeo2038](https://doi.org/10.1038/ngeo2038).
- Protti, M., F. Gundel, and K. McNally (1994). The geometry of the Wadati-Benioff zone under southern Central-America and its tectonic significance—Results from a high-resolution local seismographic network, *Phys. Earth Planet. In.* **84**, no. 1/4, 271–287.
- Reasenber, P., and D. H. Oppenheimer (1985). FPFIT, FPLOT and FPPAGE; Fortran computer programs for calculating and displaying earthquake fault-plane solutions, *Open-File Rept. VL 85-739*.
- Rietbrock, A., I. Ryder, G. Hayes, C. Haberland, D. Comte, S. Roecker, and H. Lyon-Caen (2012). Aftershock seismicity of the 2010 Maule  $M_w = 8.8$ , Chile, earthquake: Correlation between co-seismic slip models and aftershock distribution? *Geophys. Res. Lett.* **39**, no. 8, doi: [10.1029/2012GL051308](https://doi.org/10.1029/2012GL051308).
- Saikia, C. K. (1994). Modified frequency–wavenumber algorithm for regional seismograms using Filon's quadrature: Modelling of Lg waves in eastern North America, *Geophys. J. Int.* **118**, no. 1, 142–158, doi: [10.1111/j.1365-246X.1994.tb04680.x](https://doi.org/10.1111/j.1365-246X.1994.tb04680.x).
- Sato, T., S. Hiratsuka, and J. Mori (2013). Coulomb stress change for the normal-fault aftershocks triggered near the Japan trench by the 2011  $M_w$  9.0 Tohoku-Oki earthquake, *Earth Planets Space* **64**, no. 12, 1239–1243, doi: [10.5047/eps.2012.04.003](https://doi.org/10.5047/eps.2012.04.003).
- Scholz, C. (2002). *The Mechanics of Earthquakes and Faulting*, Cambridge University Press, Cambridge, United Kingdom, 471 pp.
- Stein, R. S. (1999). The role of stress transfer in earthquake occurrence, *Nature* **402**, 605–609, doi: [10.1038/45144](https://doi.org/10.1038/45144).
- Sumy, D. F., E. S. Cochran, and K. M. Keranen (2014). Observations of static Coulomb stress triggering of the November 2011  $M$  5.7 Oklahoma earthquake sequence, *J. Geophys. Res.* **119**, no. 3, 1904–1923, doi: [10.1002/2013JB010612](https://doi.org/10.1002/2013JB010612).
- Toda, S., J. Lin, and R. S. Stein (2011). Using the 2011  $M_w$  9.0 off the Pacific coast of Tohoku earthquake to test the Coulomb stress triggering hypothesis and to calculate faults brought closer to failure, *Earth Planets Space* **63**, no. 7, 725–730, doi: [10.5047/eps.2011.05.010](https://doi.org/10.5047/eps.2011.05.010).
- Toda, S., R. S. Stein, and J. Lin (2011). Widespread seismicity excitation throughout central Japan following the 2011  $M = 9.0$  Tohoku earthquake and its interpretation by Coulomb stress transfer, *Geophys. Res. Lett.* **38**, no. 7, doi: [10.1029/2011GL047834](https://doi.org/10.1029/2011GL047834).
- Toda, S., R. S. Stein, V. Sevilgen, and J. Lin (2011). Coulomb 3.3 Graphic-rich deformation and stress-change software for earthquake, tectonic, and volcano research and teaching—User guide, *U.S. Geol. Surv. Open-File Rept. 2011-1060*, 63 pp., available at <https://pubs.usgs.gov/of/2011/1060/> (last accessed August 2016).
- Trugman, D. T., and P. M. Shearer (2017). GrowClust: A hierarchical clustering algorithm for relative earthquake relocation, with application to the Spanish Springs and Sheldon, Nevada, earthquake sequences, *Seismol. Res. Lett.* **88**, no. 2A, doi: [10.1785/0220160188](https://doi.org/10.1785/0220160188).
- Waldhauser, F., and W. L. Ellsworth (2000). A double-difference earthquake location algorithm: Method and application to the northern Hayward fault, California, *Bull. Seismol. Soc. Am.* **90**, no. 6, 1353–1358, doi: [10.1785/0120000006](https://doi.org/10.1785/0120000006).
- Walter, J. I., X. Meng, Z. Peng, S. Y. Schwartz, A. V. Newman, and M. Protti (2015). Far-field triggering of foreshocks near the nucleation zone of the 5 September 2012 ( $M_w$  7.6) Nicoya Peninsula, Costa Rica earthquake, *Earth Planet. Sci. Lett.* **431**, 75–86, doi: [10.1016/j.epsl.2015.09.017](https://doi.org/10.1016/j.epsl.2015.09.017).
- Walter, J. I., S. Y. Schwartz, J. M. Protti, and V. Gonzalez (2011). Persistent tremor within the northern Costa Rica seismogenic zone, *Geophys. Res. Lett.* **38**, L01307, doi: [10.1029/2010GL045586](https://doi.org/10.1029/2010GL045586).
- Walter, J. I., S. Y. Schwartz, M. Protti, and V. Gonzalez (2013). The synchronous occurrence of shallow tremor and very low frequency earthquakes offshore of the Nicoya Peninsula, Costa Rica, *Geophys. Res. Lett.* **40**, no. 8, 1517–1522, doi: [10.1002/grl.50213](https://doi.org/10.1002/grl.50213).
- Wang, K., and S. L. Bilek (2011). Do subducting seamounts generate or stop large earthquakes? *Geology* **39**, no. 9, 819–822, doi: [10.1130/G31856.1](https://doi.org/10.1130/G31856.1).
- Xue, L., S. Y. Schwartz, Z. Liu, and L. Feng (2015). Interseismic megathrust coupling beneath the Nicoya Peninsula, Costa Rica, from the joint inversion of InSAR and GPS data, *J. Geophys. Res.* **120**, no. 5, 3707–3722, doi: [10.1002/2014JB011844](https://doi.org/10.1002/2014JB011844).
- Yue, H., T. Lay, S. Y. Schwartz, L. Rivera, M. Protti, T. H. Dixon, S. Owen, and A. V. Newman (2013). The 5 September 2012 Nicoya, Costa Rica  $M_w$  7.6 earthquake rupture process from joint inversion of high-rate GPS, strong-motion, and teleseismic  $P$ -wave data and its relationship



to adjacent plate boundary interface properties, *J. Geophys. Res.* **118**, no. 10, 5453–5466, doi: [10.1002/jgrb.50379](https://doi.org/10.1002/jgrb.50379).

Zhu, S., and M. Miao (2015). How did the 2013 Lushan earthquake ( $M_s = 7.0$ ) trigger its aftershocks? Insights from static Coulomb stress change calculations, *Pure Appl. Geophys.* **172**, no. 10, 2481–2494, doi: [10.1007/s00024-015-1064-3](https://doi.org/10.1007/s00024-015-1064-3).

Department of Earth and Planetary Sciences  
University of California Santa Cruz  
Santa Cruz, California 95064  
echavess@ucsc.edu  
sschwartz@ucsc.edu  
tlay@ucsc.edu  
(E.J.C., S.Y.S., T.L.)

Université Côte d'Azur, CNRS, OCA, IRD, Géoazur  
250 rue Albert Einstein, Sophia Antipolis 06560  
Valbonne  
France  
duboeuf@geoazur.unice.fr  
(L.D.)

Department of Geosciences  
The Pennsylvania State University  
University Park, Pennsylvania 16802  
jvk5803@psu.edu  
(J.K.)

Manuscript received 10 September 2016;  
Published Online 2 May 2017